

Local properties of the large-scale peaks of the CMB temperature

A. Marcos-Caballero,^{a,b} E. Martínez-González^a and P. Vielva^a

^aInstituto de Física de Cantabria, CSIC-Universidad de Cantabria,
Avda. de los Castros s/n, 39005 Santander, Spain.

^bDpto. de Física Moderna, Universidad de Cantabria,
Avda. los Castros s/n, 39005 Santander, Spain.

E-mail: marcos@ifca.unican.es, martinez@ifca.unican.es, vielva@ifca.unican.es

Abstract. In the present work, we study the largest structures of the CMB temperature measured by Planck in terms of the most prominent peaks on the sky, which, in particular, are located in the southern galactic hemisphere. Besides these large-scale features, the well-known Cold Spot anomaly is included in the analysis. All these peaks would contribute significantly to some of the CMB large-scale anomalies, as the parity and hemispherical asymmetries, the dipole modulation, the alignment between the quadrupole and the octopole, or in the case of the Cold Spot, to the non-Gaussianity of the field. The analysis of the peaks is performed by using their multipolar profiles, which characterize the local shape of the peaks in terms of the discrete Fourier transform of the azimuthal angle. In order to quantify the local anisotropy of the peaks, the distribution of the phases of the multipolar profiles is studied by using the Rayleigh random walk methodology. Finally, a direct analysis of the 2-dimensional field around the peaks is performed in order to take into account the effect of the galactic mask. The results of the analysis conclude that, once the peak amplitude and its first and second order derivatives at the centre are conditioned, the rest of the field is compatible with the standard model. In particular, it is observed that the Cold Spot anomaly is caused by the large value of curvature at the centre.

Contents

1	Introduction	1
2	Characterization of the large-scale peaks	2
3	Multipolar profiles	5
4	Phase correlations of the multipolar profiles	8
5	Real space analysis	13
6	Conclusions	14
A	Binning of the theoretical profiles	16

1 Introduction

The anisotropies in the Cosmic Microwave Background (CMB) are described inside the standard model of cosmology, which assumes that the initial perturbations are distributed according to a Gaussian in a homogeneous and isotropic Universe. The recent measurements of the CMB allow one to determine the cosmological parameters with high precision [1], showing an overall agreement between data and the concordance cosmological model. Although, in general, this agreement is large, some anomalies are found in the CMB at large scales. The characterization of these deviations have an important role in understanding the process which leads to the initial perturbations, and hence, in the characterization of the inflationary model.

Different large-scale anomalies are found in the CMB, which were first detected in the WMAP data ([2], see also references below) and confirmed later by Planck [3]. Among them, it is included the lack of correlations on large scales [4, 5] which might leads to a low variance in the temperature field [6]. In particular, in terms of the angular power spectrum, the low variance anomaly can be seen as a deficit of power in the lowest multipoles, in particular in the quadrupole and octopole [7]. Explanations in terms of an early fast-roll phase of the inflation field preceding the standard slow-roll phase have been proposed [8, 9].

On the other hand, when the temperature field is expanded in terms of the spherical harmonics, an unlikely alignment between the quadrupole and the octopole is observed [10, 11]. The interference between the two multipoles produce large-scale features in the CMB temperature aligned with the ecliptic plane, which, in particular, have more power in the southern hemisphere. The hemispherical asymmetry, which is seen in the low multipoles range ($\ell \leq 64$), was first detected in [12] by looking at the ratio of the power spectrum amplitude calculated on opposing hemispheres, and later extended to include smaller scales in [13]. This particular asymmetry axis is also found in the dipole modulation, which has been studied in real space [14, 15], as well as in harmonic space in order to take into account the scale dependence in the analysis [3].

Moreover, parity asymmetries have been also analysed concluding that there exists a difference in the variance of the odd and even components of the temperature field [16–18].

These studies have been extended including a directional dependence in the parity asymmetry estimator in several works [19, 20], indicating that the preferred axis for parity violations could correspond to the quadrupole and octopole alignment direction. Since the parity asymmetry measures the correlation between antipodal points on the sphere, this anomaly can be related to the lack of power at large scales [21].

In the present paper, we study the large-scale features on the CMB temperature by identifying the most prominent peaks and analysing their statistical properties. These largest peaks correspond to structures located in the galactic southern hemisphere, more precisely, in the quadrant where the south ecliptic pole is located. This region of the sky corresponds to the direction where some of the above mentioned anomalies are located (power asymmetry or dipole modulation). Besides this directional asymmetries, the interference of the quadrupole and the octopole induces an excess of power in the ecliptic southern hemisphere which is caused by their particular alignment [22]. Additionally, although it is not a peak as large as the others we consider, the Cold Spot [23, 24] is also included in the analysis since it presents an anomalous peak curvature. All these structures correspond in part to the “fingers” and spots studied in [25]. Moreover, in a recent paper [26], a multiscale analysis reveals that these peaks are the most outstanding large-scale deviations in terms of either the amplitude or the curvature.

The paper is organized as follows: in Section 2, the large-scale peaks are selected in the temperature field, characterizing their local shape through the derivatives up to second order. The analysis of the peaks is performed in terms of the radial shape of the multipolar profiles in Section 3, whereas the study of their phase correlations is considered in Section 4. In order to implement a partial sky coverage properly, the work is completed with an analysis of the peaks directly in real space. Finally, the summary and conclusions of the paper are outlined in Section 6.

2 Characterization of the large-scale peaks

The peaks in the CMB correspond to local maxima or minima in the temperature field, and they had been considered as useful geometrical descriptors of the statistical properties of the primordial radiation [27–31]. In order to have an extremum, constraints on the field derivatives have to be imposed. Firstly, the critical point condition implies that the gradient of the temperature must vanish at the peak location, but additionally, in order to exclude possible saddle points, it is imposed that the Hessian matrix is positive or negative definite, depending whether the extremum is a minimum or a maximum. Therefore, it is natural to characterize the peaks theoretically by conditioning the first and second derivatives at the centre of the peak, as well as the corresponding peak height. Following the notation in [31], the derivatives on the sphere are calculated by using the spin raising and lowering operators:

$$\nu = \frac{T}{\sigma_\nu}, \quad (2.1a)$$

$$\eta = \frac{\not{\partial}^* T}{\sigma_\eta}, \quad (2.1b)$$

$$\kappa = -\frac{\not{\partial}^* \not{\partial} T}{\sigma_\kappa}, \quad (2.1c)$$

$$\epsilon = \frac{(\not{\partial}^*)^2 T}{\sigma_\epsilon}, \quad (2.1d)$$

where the derivatives are normalized in order to have dimensionless quantities with unit variance. This set of parameters corresponds to our peak degrees of freedom, which consist in two scalars (ν and κ), one vector (η) and one 2-spinor (ϵ). Whilst the value of the temperature at the extremum is given by the peak height ν , the local curvature is described by the Laplacian, which is proportional to κ . On the other hand, the spinorial quantities η and ϵ represent the gradient and the eccentricity tensor, respectively. The components of these two spinors expressed in the helicity basis are given by complex numbers, whose real and imaginary parts describe geometrical aspects of the peak. For instance, the local eccentricity of the peak is proportional to the modulus of ϵ , whereas its phase represents the particular direction of the principal axes on the sky. Regarding the gradient, the real and imaginary parts of η correspond to the components of the first derivatives in the orthogonal local system of reference. Theoretically, the gradient at the peak location must vanish by definition, but we maintain this degree of freedom as non-zero in the formalism because, in practice, there is a residual gradient due to the fact that we are selecting peaks as local extrema in a discretised field, which prevents us to impose $\eta = 0$. Although this non-null value of the first derivative is very small compared to its standard deviation, analysis based on conditioning the derivatives are very sensitive to small variations of the conditioned values. In terms of the peak shape, this effect causes a dipolar asymmetry at distances larger than the peak size (see figure 8 in Section 5).

In this work, we consider the five large-scale peaks given in figure 1. In a recent paper [26], a complete analysis of deviations on the derivatives fields is performed at different scales, concluding that these peaks are the most anomalous structures at large scales. The peaks labeled by 1-4 correspond to two maxima and two minima selected in the CMB temperature field filtered with a Gaussian with $R = 10^\circ$. These peaks are the most prominent large-scale structures in the sky, which are located in the same ecliptic hemisphere. The particular value of $R = 10^\circ$ is chosen so that these large-scale fluctuations are highlighted. On the other hand, the peak labeled by 5 is the well-known CMB anomaly called the Cold Spot [24], which is included in the analysis because is the most outstanding large-scale deviation in terms of the curvature [26], contributing to the non-Gaussianity of the temperature field [23, 24]. The Cold spot is usually characterized as a minimum in the Spherical Mexican Hat Wavelet (SMHW) [32] coefficient map at the scale $R \approx 5^\circ$. As the SMHW is obtained from the Laplacian of the Gaussian function, the coefficients map is equivalent to the curvature field κ of the temperature, filtered with a Gaussian with the same scale than the SMHW. Since there is a strong correlation between ν and κ at large scales, a minimum in the curvature corresponds to a minimum in the temperature field itself. For this reason, we equivalently define the Cold Spot as a minimum in ν at the scale $R = 5^\circ$.

In order to calculate the variances of the derivatives and other theoretical quantities, a particular model has to be considered. The following fiducial model is assumed: $\Omega_b h^2 = 0.2222$, $\Omega_c h^2 = 0.1197$, $H_0 = 67.31$ km/s Mpc $^{-1}$, $\tau = 0.078$, $n_s = 0.9655$ and $\ln(10^{10} A_s) = 3.089$, which represent the Planck TT-lowP best-fit cosmological parameters ([1], table 3).

The values of the derivatives at the centre of the peaks obtained from the Planck Commander map [33] are represented in figure 2. The scalar degrees of freedom ν and κ are depicted in the same plane, showing the contours of the one-point probability density function. Since the correlation between ν and κ depend on the scale where the peak is selected, it is expected that the ellipses for the peaks 1-4 ($R = 10^\circ$) are narrower than the ones for the peak 5, whose scale is smaller ($R = 5^\circ$). On the other hand, the one-point distribution of the eccentricity tensor does not depend on the scale R [31], and therefore the probability

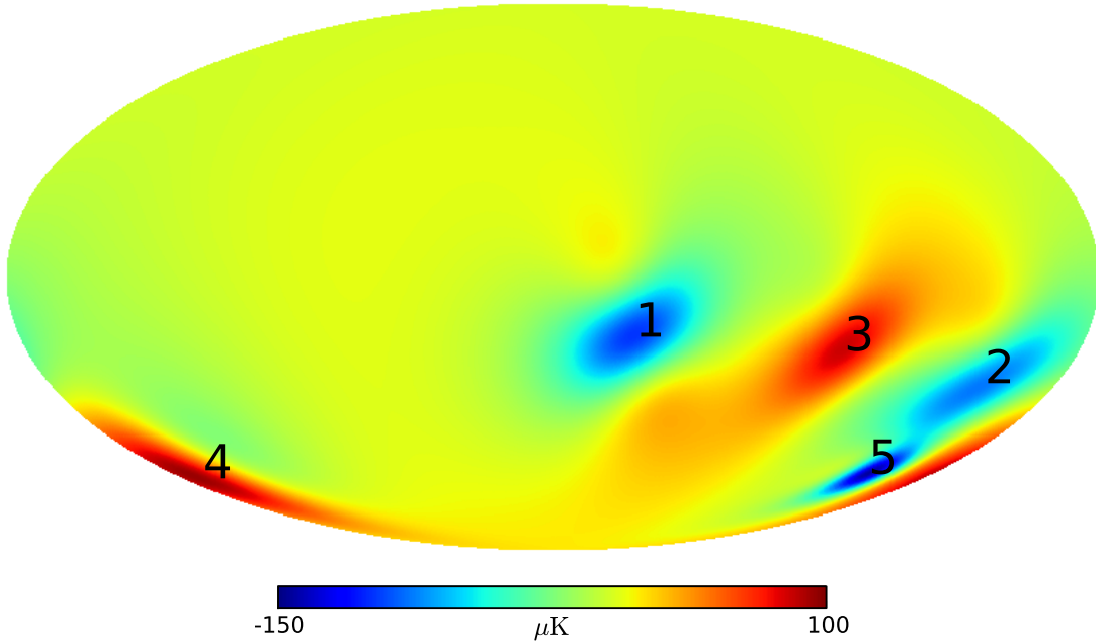


Figure 1. Locations of the large-scale peaks considered in the paper, which are labeled with the numbers as referred in the text. The color map represents the theoretical mean field produced by conditioning the derivatives at the centre of the peaks. Notice that the correlation between peaks are not taken into account in this figure, causing that the derivatives do not correspond exactly to the observed values.

contours are the same of all the peaks. The Cold Spot (peak 5) is the peak which presents a higher deviation in the ν - κ plane, mainly caused by the large value of $\kappa \approx 4$. This value differs from the SMHW coefficient $\kappa \approx 4.7$ reported in [24] and confirmed by [3] for the same scale, giving a lower probability of finding a Cold Spot in the CMB temperature. The main difference between these calculations is that, whereas in this work the value of κ is calculated by normalizing by the theoretical variance σ_κ , in [24] and [3] the value of the SMHW coefficient is calculated by using the variance estimated from the data, which is affected by the low variance of the measured CMB field at large scales [3, 6]. On the other hand, the eccentricity of the Cold Spot is within the 2σ level, which implies that its shape is almost circular [34].

The deviation of the peaks derivatives with respect to the standard model is considered by calculating the expected number of peaks with ν and κ as extreme as the corresponding observed values which are present in one realization of the temperature field (see [31] for the expression of the number density of peaks on the sphere). These numbers are 0.054 for the Cold Spot and 0.14 for the largest cold spot at $R = 10^\circ$ (peak 1), whereas the rest of the peaks have an expected number per realization ≈ 1 . This implies that a peak as extreme as the Cold Spot in terms of ν and κ is expected in every 19 realizations of the CMB temperature, given a more likely probability for the Cold Spot than the calculation in [24], which considers a larger value for the curvature κ at the centre of the peak, as explained above.

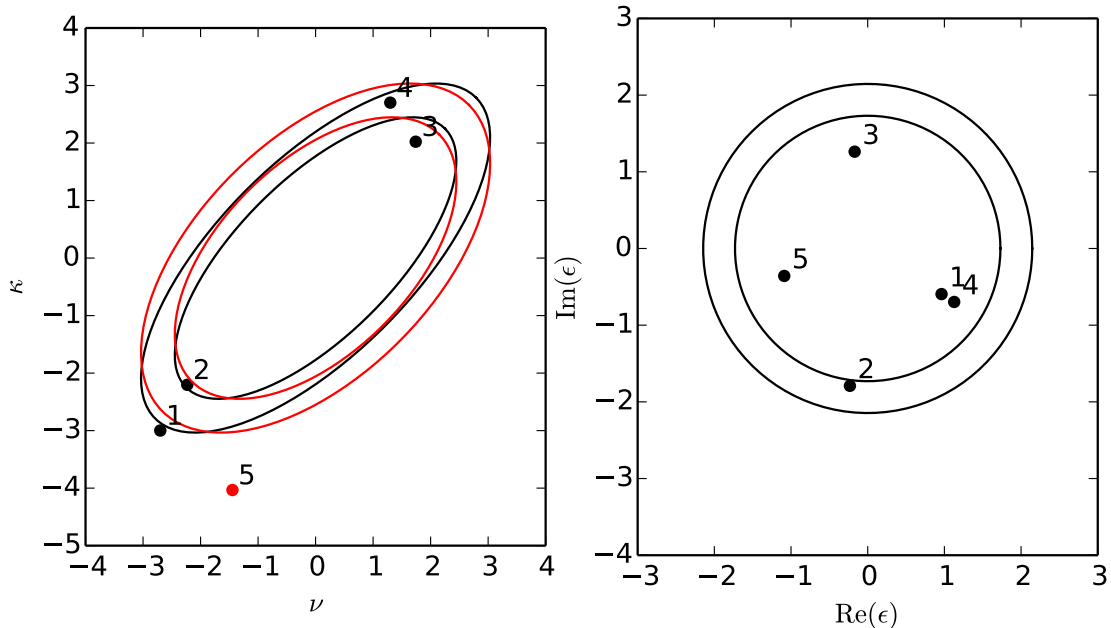


Figure 2. The peak degrees of freedom labeled with the numbers which identify each peak throughout the paper. Whilst the peak height ν and the curvature κ are shown in the left panel, the values of the eccentricity tensor ϵ are depicted in the complex plane in the right panel. The ellipses represent the probability contours at 95% and 99% levels. In the case of the ν - κ plane, the contours for the peaks 1-4 are represented in black, and the corresponding ellipses for the Cold Spot (peak 5) are shown in red.

3 Multipolar profiles

In this section, we study the shape of the largest peaks observed in the CMB temperature. Following the formalism of [31], the shape of the peaks can be studied through the multipolar profiles, which consist in the coefficients of the Fourier transform of the azimuthal angle around the peak:

$$T_m(\theta) = \frac{1}{2\pi} \int d\phi T(\theta, \phi) e^{-im\phi} , \quad (3.1)$$

where the coordinates θ and ϕ represent the radial and azimuthal coordinates, respectively, centered at the peak location. The monopolar profile with $m = 0$ corresponds to the standard profile, which takes into account the spherical symmetric component of the peak. On the other hand, the higher order profiles describe different asymmetrical shapes, depending on the multipole m . For instance, the profiles with $m = 1$ and $m = 2$ represent a dipole and a quadrupole around the peak, respectively.

The derivatives at the centre of the peak affects to the local shape depending on its spin. In particular, if the values of ν , κ , η and ϵ are fixed at the centre, it is obtained the following mean profiles [31]:

$$\langle T_0(\theta) \rangle = \sum_{\ell=0}^{\infty} \frac{2\ell+1}{4\pi} [b_\nu + b_\kappa \ell(\ell+1)] b_\ell w_\ell C_\ell P_\ell(\cos \theta) , \quad (3.2a)$$

$$\langle T_1(\theta) \rangle = b_\eta \sum_{\ell=0}^{\infty} \frac{2\ell+1}{4\pi} b_\ell w_\ell C_\ell P_\ell^1(\cos\theta) , \quad (3.2b)$$

$$\langle T_2(\theta) \rangle = b_\epsilon \sum_{\ell=0}^{\infty} \frac{2\ell+1}{4\pi} b_\ell w_\ell C_\ell P_\ell^2(\cos\theta) , \quad (3.2c)$$

and $\langle T_m(\theta) \rangle = 0$ for $m \neq 0, 1, 2$. In these equations, we have assumed that the peak is selected in the temperature field filtered with the window function w_ℓ , whereas the profiles are calculated from a field observed with a beam b_ℓ . The bias parameters characterizing the mean profiles depend on the particular values of the derivatives at the centre:

$$b_\nu = \frac{\nu - \rho\kappa}{\sigma_\nu(1 - \rho^2)} , \quad (3.3a)$$

$$b_\kappa = \frac{\kappa - \rho\nu}{\sigma_\kappa(1 - \rho^2)} , \quad (3.3b)$$

$$b_\eta = \frac{\eta}{\sigma_\eta} , \quad (3.3c)$$

$$b_\epsilon = \frac{\epsilon}{\sigma_\epsilon} , \quad (3.3d)$$

where ρ is the correlation coefficient between ν and κ . As it is mentioned before, despite the fact that we are selecting maxima and minima, the gradient at peak location does not vanish because of the discretization of the field. This particular residual affecting to the dipolar profile can be modelled as a small bias b_η depending on the measured value of η . This simple modelization of the bias is enough to correct all the systematic effect appearing in the subsequent analysis.

Additionally, when the local shape of the peak is fixed, the covariance of the multipolar profiles are given by [31]:

$$\langle T_m(\theta) T_{m'}^*(\theta') \rangle = \langle T_m(\theta) T_{m'}^*(\theta') \rangle_{\text{intr.}} + \langle T_m(\theta) T_{m'}^*(\theta') \rangle_{\text{peak}} . \quad (3.4)$$

Whilst the intrinsic part $\langle T_m(\theta) T_{m'}^*(\theta') \rangle_{\text{intr.}}$ represents the covariance of the profile when the derivatives at the centre are not constrained, the term $\langle T_m(\theta) T_{m'}^*(\theta') \rangle_{\text{peak}}$ is the modification of the covariance due to the fact of conditioning the values of the derivatives. It is important to notice that the fact of conditioning the derivatives to some particular values only affects to the mean profiles, but not to the covariance. The intrinsic covariance can be calculated from the angular power spectra in the following way [31]:

$$\langle T_m(\theta) T_{m'}^*(\theta') \rangle_{\text{intr.}} = \delta_{mm'} \sum_{\ell=m}^{\infty} \frac{2\ell+1}{4\pi} \frac{(\ell-m)!}{(\ell+m)!} b_\ell^2 C_\ell P_\ell^m(\cos\theta) P_\ell^m(\cos\theta') = \delta_{mm'} C_m^{\text{intr.}}(\theta, \theta') . \quad (3.5)$$

On the other hand, the contribution of the peak to the covariance of the multipolar profiles is different from zero for $m = 0, 1, 2$. In general, it can be written as:

$$\begin{aligned} \langle T_m(\theta) T_{m'}^*(\theta') \rangle_{\text{peak}} &= \delta_{mm'} \sum_{\ell, \ell'=m}^{\infty} \frac{2\ell+1}{4\pi} \frac{2\ell'+1}{4\pi} B_{\ell\ell'}^m b_\ell w_\ell C_\ell b_{\ell'} w_{\ell'} C_{\ell'} P_\ell^m(\cos\theta) P_{\ell'}^m(\cos\theta') = \\ &= \delta_{mm'} C_m^{\text{peak}}(\theta, \theta') , \end{aligned} \quad (3.6)$$

where the matrices $B_{\ell\ell'}^m$ are given by:

$$B_{\ell\ell'}^0 = -\frac{1}{1-\rho^2} \left\{ \frac{1}{\sigma_\nu^2} - \frac{\rho}{\sigma_\nu\sigma_\kappa} [\ell(\ell+1) + \ell'(\ell'+1)] + \frac{\ell(\ell+1)\ell'(\ell'+1)}{\sigma_\kappa^2} \right\}, \quad (3.7a)$$

$$B_{\ell\ell'}^1 = -\frac{1}{\sigma_\eta^2}, \quad (3.7b)$$

$$B_{\ell\ell'}^2 = -\frac{1}{\sigma_\epsilon^2}, \quad (3.7c)$$

and $B_{\ell\ell'}^m = 0$ for $m > 2$. Since conditioning the derivatives reduces the variance of the field, these coefficients are always negative. These expressions can be generalised to consider scenarios where only the amplitude or the curvature are conditioned. In this case, we have that $B_{\ell\ell'}^0$ equals to $-\sigma_\nu^{-2}$ or $-\sigma_\kappa^{-2}$, depending on whether ν or κ is the conditioned variable.

As it is described in Section 2, the peaks 1-4 are selected in a map filtered with a Gaussian with a scale $R = 10^\circ$, whereas the Cold Spot is defined as a peak in $R = 5^\circ$. Therefore, the window function w_ℓ , which characterizes the smoothing of the field where the amplitude and its derivatives are calculated, is a Gaussian filter whose scale R depends on the peak considered. On the other hand, the filter b_ℓ corresponds to the effective resolution of the maps over which the multipolar profiles are calculated.

In order to analyse the shape of the peaks, the values of ν , κ , η and ϵ are conditioned to the measured values at the centre of the peak. The observed monopolar, dipolar and quadrupolar profiles are compared with the theoretical predictions in figures 3-5. In the case of the quadrupolar profile, a rotation is performed in order to align the principal axes with the system of reference of the peak, such that only the real part has non-zero expectation value. Statistical deviations from the standard model are quantified using a χ^2 test as a function of the maximum value of θ considered in the analysis. Assuming that the CMB temperature is a Gaussian random field, the conditional probability of the multipolar profiles obtained fixing the values of the derivatives at the centre is also Gaussian, therefore the χ^2 test is appropriate for the analysis. It is computed the following quantity for each χ^2 value, which is approximately normally distributed for a large number of degrees of freedom:

$$z_m(\theta_{\max}) = \frac{\chi_m^2(\theta_{\max}) - n_f(\theta_{\max})}{\sqrt{2n_f(\theta_{\max})}}, \quad (3.8)$$

where θ_{\max} represents the maximum value of θ considered in the test, and n_f is the number of degrees of freedom of the χ^2 variable corresponding to that value of θ_{\max} . Whereas for $m = 0$ the value of n_f is equal to the number of bins considered, for any other multipole m it is twice the number of bins due to the fact that the profiles take complex values. In this equation, the statistics $\chi_m^2(\theta_{\max})$ is computed from the measured profiles and the theoretical mean profiles and covariances:

$$\chi_m^2(\theta_{\max}) = (2 - \delta_{m0}) \sum_{\theta_i, \theta_j \leq \theta_{\max}} [T_m^*(\theta_i) - \langle T_m^*(\theta_i) \rangle] C_m^{-1}(\theta_i, \theta_j) [T_m(\theta_j) - \langle T_m(\theta_j) \rangle], \quad (3.9)$$

where the matrix $C_m(\theta_i, \theta_j) = C_m^{\text{intr.}}(\theta_i, \theta_j) + C_m^{\text{peak}}(\theta_i, \theta_j)$ is the covariance between the different bins of the multipolar profiles, which is given by the sum of eq. (3.5) and eq. (3.6). The summations in this expression are extended over the indices for which the centre of the bins θ_i take values up to the θ_{\max} . Regarding the theoretical estimation, the mean profiles

and covariance must be also averaged in each bin in order to compare with the data. This operation is equivalent to calculate the integral of the associated Legendre functions in each interval of θ . In the literature [35], there exists analytical formulae which allow to calculate these integrals recursively (see appendix A). Notice that both the real and the imaginary parts of the multipolar profiles $T_m(\theta)$ are considered in the calculation of $\chi_m^2(\theta_{\max})$. Commonly, the peaks are oriented along the principal axes, in which case the mean value of the imaginary parts vanishes.

Since we are interested in large-scale peaks, the galactic mask is a problem in the calculation of the profiles, specially in the ones with $m > 0$, where the break of the isotropy of the field is critical. Deconvolution techniques based on the Toeplitz matrix can be used in order to correct the mask effect, but in the case of aggressive masking the resulting profiles are not accurately calculated. For this reason, we use an inpainted map without missing pixels, more precisely, the CMB temperature field used in the analysis of the multipolar profiles is the Planck Commander map [33], whose galactic mask region has been filled by calculating a constrained Gaussian realization. On the other hand, in Section 5, the peaks are analysed directly in real space, where the missing pixels are not problematic, and therefore the inpainting techniques are not required.

Following the expression in eq. (3.1), the multipolar profiles are calculated by averaging the pixels in rings whose width is 1° and are centred at the different values of θ . Since the size of these bins is large compared with the resolution of the Planck Commander map (FWHM $5'$), the contribution of the instrumental noise can be ignored in our analysis. On the other hand, the filter b_ℓ used in the calculation of the theoretical profiles and covariance is the product of a Gaussian filter characterizing the resolution of the data and the corresponding pixel window function.

In figures 3-5, it is represented the values of $z(\theta_{\max})$ for the monopolar, dipolar and quadrupolar profiles, respectively. We can see that the deviation of these profiles is less than 2σ in all the peaks considered. Moreover, the multipolar profiles with values of m up to 10 have been analysed, obtaining values which are compatible at 3σ level with what is expected in the standard model.

Particularly, in the Cold Spot analysis, it is found that the monopolar profile agrees with the standard model prediction when the values of ν and κ are conditioned. On the other hand, if only the value of ν is fixed to the observed value whereas κ is averaged out using its probability density distribution (see [31]), the Cold Spot profile presents a 4.7σ deviation for $\theta < 10^\circ$. This result implies that the Cold Spot anomaly is mainly caused by the extremely large value of κ at the centre, whereas when κ is conditioned, no anomaly is found in the monopolar profile. In figure 6, it is represented the monopolar profiles of the Cold Spot obtained by conditioning, the peak height ν , the curvature κ , or both. Notice that the ring-shape in the Cold spot at $\approx 15^\circ$ is only recovered when both degrees of freedom are fixed, which implies that this distinctive feature is produced by a combined effect of a large value of κ with a relatively small absolute value of ν .

4 Phase correlations of the multipolar profiles

In order to detect deviations from the standard model, the statistical properties of the phases of the spherical harmonics coefficients have been studied in several works. If the CMB temperature field is non-Gaussian or anisotropic, correlations in the phases of the $a_{\ell m}$'s may exist, which causes that they are not uniformly distributed in the interval $[0, 2\pi]$. There

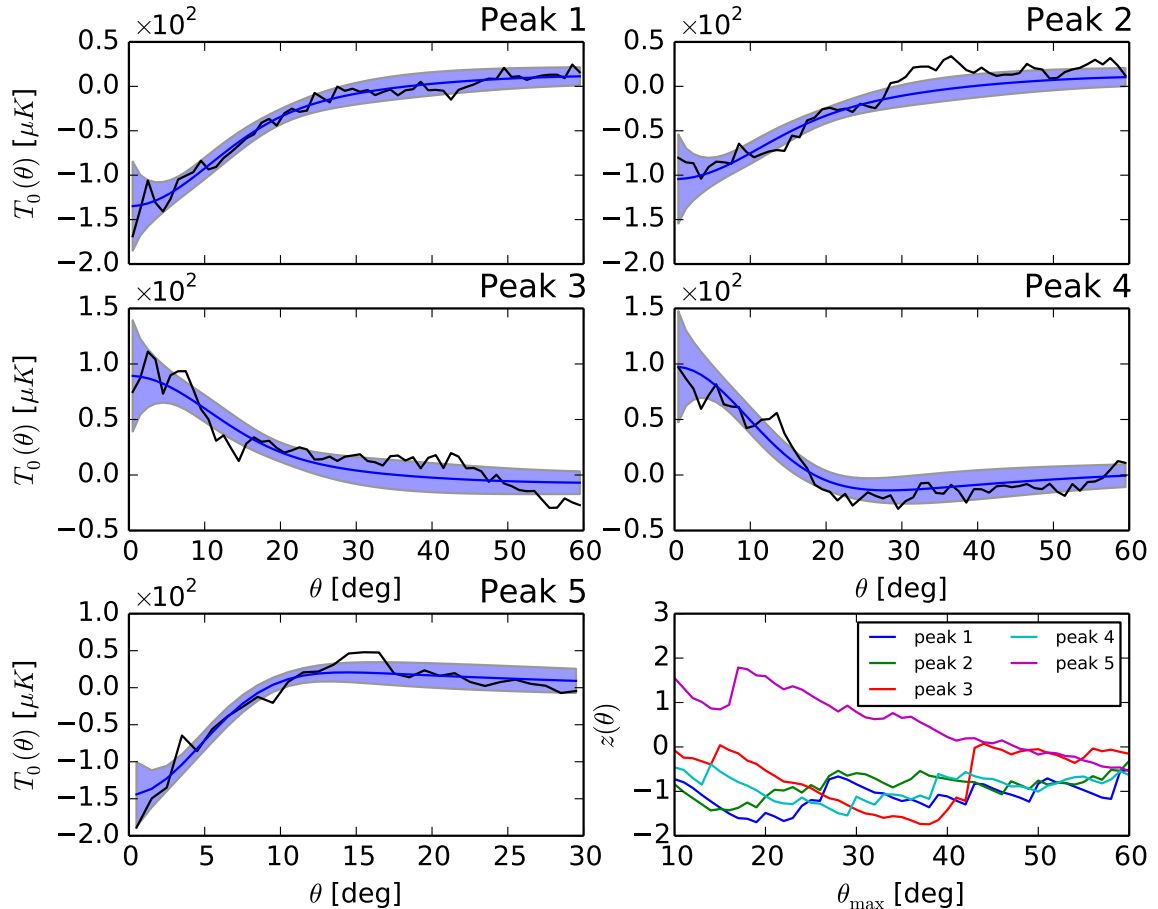


Figure 3. Monopolar profiles ($m = 0$) and their fit parameters z (see the text for details) for the different peaks considered. The blue line represents the theoretical mean profiles conditioned to the values of ν and κ at $\theta = 0$ observed for each peak, and the shaded regions show the 1σ error bars. The fit parameter z is depicted as a function of θ_{\max} , the maximum value of θ of the profile considered in the fit.

are different statistical tests which can be applied to study the randomness of this kind of periodic variables. For instance, the Kuiper’s test, which is a generalization of the KS test for circular data, has been used in the analysis of the phases [36]. On the other hand, in [37], the study of the Rayleigh statistics and the random walk performed by the $a_{\ell m}$ ’s in the complex plane are applied to the CMB temperature data. All the analyses considered in these works are based on the spherical harmonics coefficients, which describe the field in a particular system of reference, and therefore their results could depend on the direction of the z axis. Additionally, in a previous work [38], the genus of the largest structures on the CMB ($\ell \leq 8$) are analysed concluding that they corresponds to the ones derived from Gaussian field with random phases. In the following, the phases of the multipolar expansion centred at different peak locations are studied in terms of the multipolar profiles.

The decomposition of the field around the peaks in terms of the profiles $T_m(\theta)$ gives information about the contribution of each multipolar pattern to the peak shape. In particular, the phases of the multipolar profiles represent the orientation of each multipole in the local

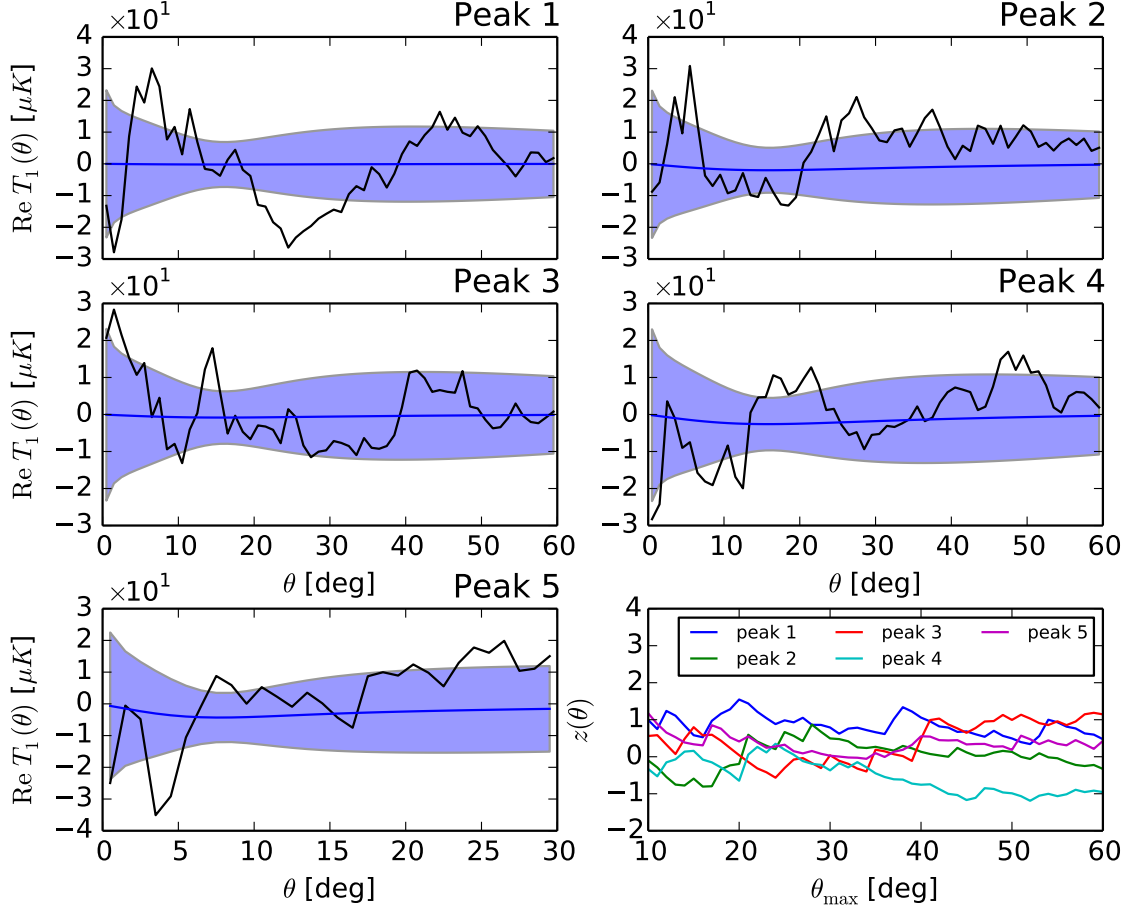


Figure 4. Real part of the dipolar profiles ($m = 1$) once the peaks are oriented in the direction of the residual gradient introduced by the pixelization. The blue line represents the theoretical mean profiles conditioned to the value of η at $\theta = 0$ observed for each peak, and the shaded regions show the 1σ error bars. Additionally, the fit parameter z is depicted as a function of θ_{\max} , the maximum value of θ considered in the fit.

system of reference centred at the peak. Given a multipole m , the phases of $T_m(\theta)$ for different values of θ are not independent due to the intrinsic correlations in the field, and therefore an alignment of the multipoles is expected. In order to test whether these correlations follow the standard model or not, profiles whose bins in θ are independent are defined. More precisely, considering n bins of the radial angle labeled by θ_a , the following profiles are calculated:

$$\hat{T}_m(\theta_a) = \sum_{b=1}^a \lambda_{ab}^m [T_m(\theta_b) - \langle T_m(\theta_b) \rangle] , \quad (4.1)$$

where the coefficients λ_{ab}^m are chosen such that $\hat{T}_m(\theta_a)$ have unit variance and no correlation for different values of a . In practice, for each value of m , the coefficients λ_{ab}^m correspond to the components of the lower triangular matrix obtained from the Cholesky decomposition of the inverse covariance given in eq. (3.4). Additionally, the mean profile $\langle T_m(\theta_b) \rangle$ is subtracted to the data in eq. (4.1) in order to remove the peak degrees of freedom from the phases analysis, since otherwise the phases can be correlated because we are centred in a particular point of

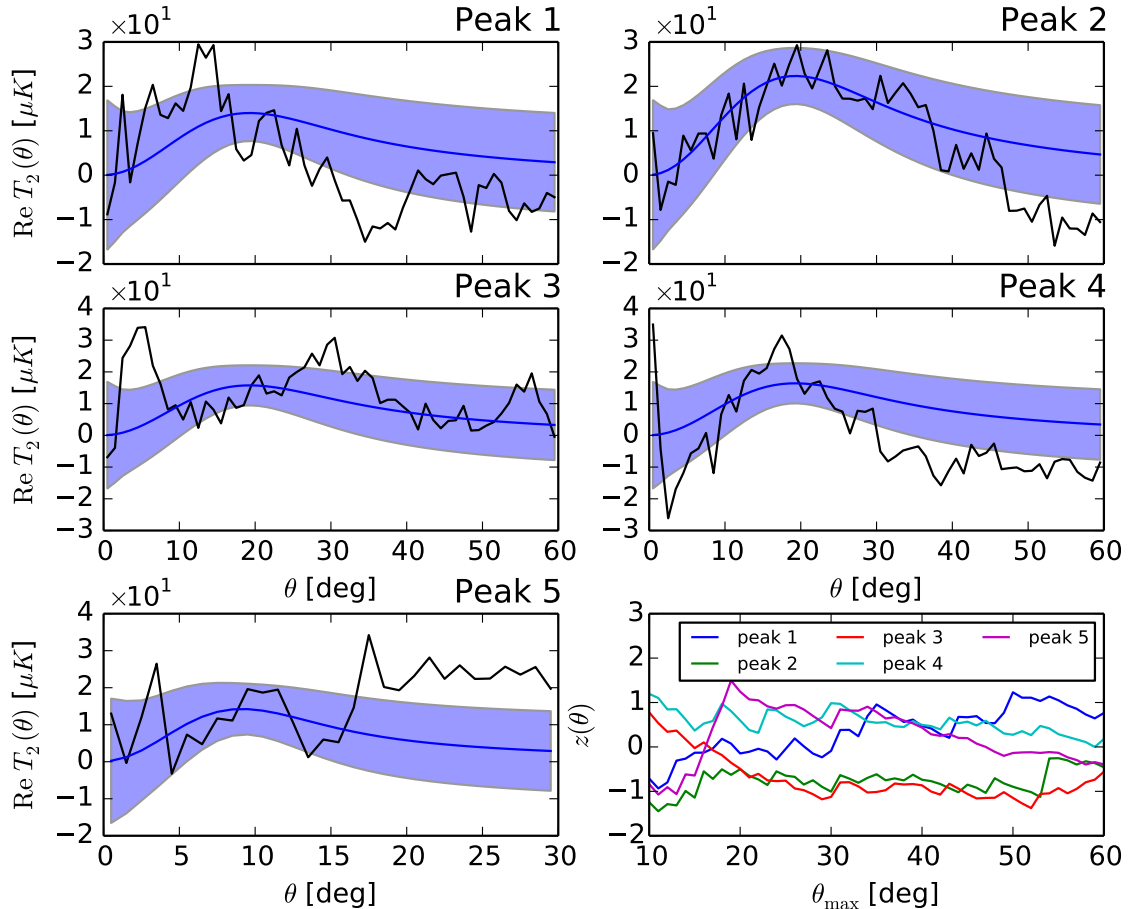


Figure 5. Real part of the quadrupolar profiles ($m = 2$) oriented along the principal axis for the different peaks considered. The blue line represents the theoretical mean profiles conditioned to the value of ϵ at $\theta = 0$ observed for each peak, and the shaded regions show the 1σ error bars. Additionally, the fit parameter z is depicted as a function of θ_{\max} , the maximum value of θ considered in the fit.

the field with a peak. Notice that the cumulative sum in eq. (4.1) implies that $\hat{T}_m(\theta_a)$ only depends on the values of the temperature with radial distance from the peak centre smaller than θ_a .

As the phases of $\hat{T}_m(\theta_a)$ are independent, they describe a Rayleigh random walk in the complex plane for each value of m . At the time step N , the position of this random walk is given by

$$Z_N^m = \sum_{a=1}^N \frac{\hat{T}_m(\theta_a)}{|\hat{T}_m(\theta_a)|}. \quad (4.2)$$

In these models of random walks, the time step N corresponds to the maximum radial angle θ_N considered in the multipolar profile. Notice that, if a rotation of the system of reference around the peak is performed with an angle α , the positions of the random walk transform as $Z_N^m e^{im\alpha}$, as can be deduced from the transformation properties of the multipolar profiles. This is just a rotation of angle $m\alpha$ of the complex plane where the random walk moves on. Since the action of the rotation group on the steps Z_N^m is different for each value of m , we

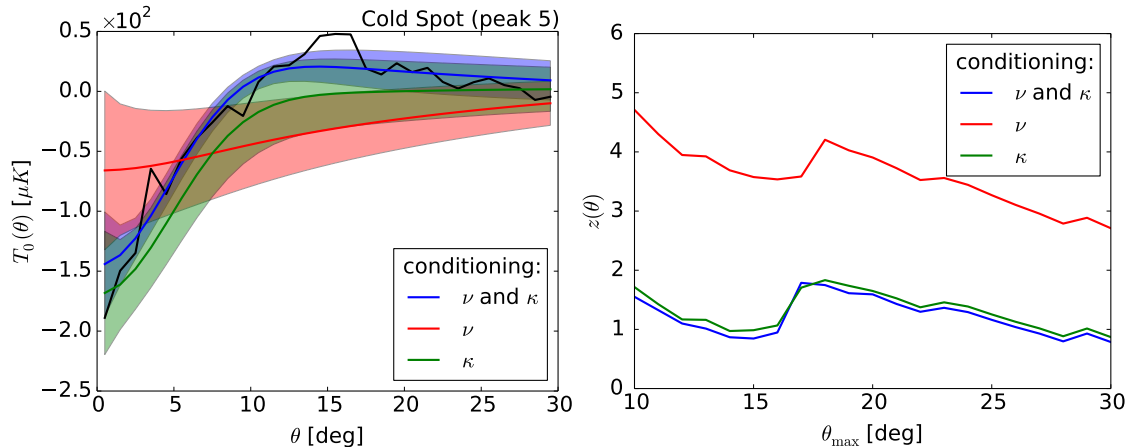


Figure 6. *Left:* Monopolar profiles of the Cold Spot obtained by conditioning the amplitude ν , the curvature κ , or both. The shaded region represent the 1σ error bar in each case. *Right:* χ^2 test performed over these profiles measured in terms of the normal variable z as a function of the maximum value of θ considered in the analysis.

consider a random walk for different multipolar profile separately. In previous works [37] based on the spherical harmonics coefficients, different values of m contribute to the steps, which implies that the resulting random walk analysis is not invariant under rotations of the z axis. On the other hand, in the scenario considered in this paper, the analysis of the random walks performed by the phases of each multipolar profile only depends on the position of the peak, and not on the orientation of the local system of reference.

The distance between the random walk position at the step N and the origin of the complex plane is approximately distributed following the probability density

$$P_N(r) = \frac{2r}{N} e^{-r^2/N}, \quad (4.3)$$

which is valid for large values of N . From this equation, it can be deduced that the variable $\sqrt{2/N}r$ is distributed according to the Rayleigh distribution (or equivalently, $2r^2/N$ follows a χ^2 with two degrees of freedom). In order to achieve better precision with this formula, the value of r is calculated as follows [39]:

$$r_N^m = \sqrt{\left(1 - \frac{1}{2N}\right) |Z_N^m|^2 + \frac{|Z_N^m|^4}{4N^2}}. \quad (4.4)$$

For large values of N , the variable r_N^m approach to the distance travelled by the random walk $|Z_N^m|$. Considering this definition, the variable r_N^m follows the probability in eq. (4.3) with $O(N^{-2})$ accuracy, instead of the $O(N^{-1})$ error achieved with the standard definition of the distance ($r_N^m = |Z_N^m|$).

The analysis is based on the fact that if the phases of the profiles $\hat{T}_m(\theta_a)$ are correlated, the distances travelled by the random walks will be greater than the ones expected from eq. (4.3). The paths followed by the random walks obtained from the phases of the multipolar profiles of the different peaks considered are represented in figure 7. In addition, the lower tail probability of the distance travelled by the random walk at the time step N is depicted.

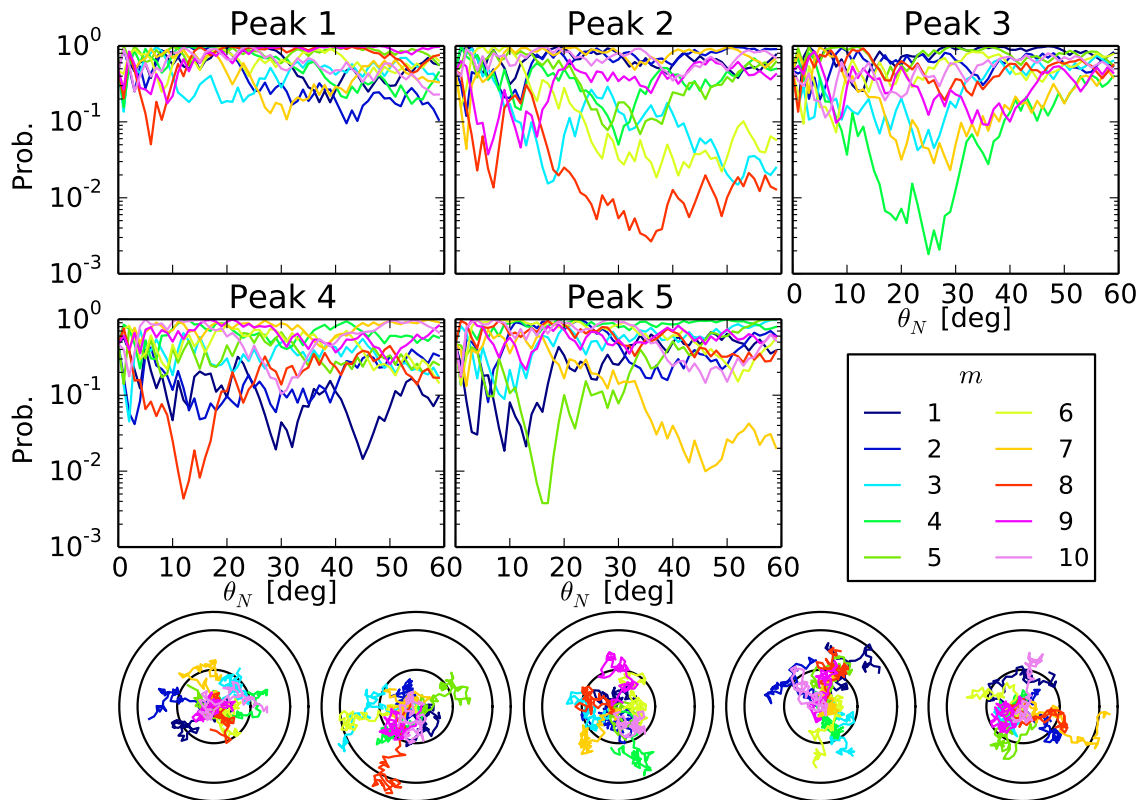


Figure 7. *First and second rows:* Lower tail probabilities of the distance travelled by the Rayleigh random walks Z_N^m as a function of the time step N , which corresponds to the angle θ_N as labeled in the x axis. Different colours represent the multipole m of the profile as described in the legend. *Bottom row:* Paths followed by the Rayleigh random walks derived by the phases of the multipolar profiles of the large scale peaks considered in the paper (numbers of the peaks are ordered from left to right). The black solid circles define the positions at which the probability distribution of the total travelled distance takes the values 0.50, 0.95 and 0.99, from inner to the outer circle.

It is possible to see some evidences of correlation of the phases for the multipole $m = 8$ in the peaks 2 and 4, whereas in the case of the peaks 3 and 5, the most correlated multipoles are $m = 4$ and $m = 5$, respectively. Regarding the Cold Spot (peak 5), it is important to notice that the maximum correlation is reached at $\approx 15^\circ$, the angular distance which coincides with the position of a hot ring around the centre of the Cold Spot. On the other hand, the lack of anomalies in this analysis can be seen as evidence of the low level of residuals in the Planck Commander map at full-sky.

5 Real space analysis

In the case of having an incomplete sky, the multipolar profiles with $m \neq 0$ are very sensitive to the geometry of the mask. This is not the case of the monopolar profiles ($m = 0$), for which the standard sky fraction correction is enough to have a good estimation of the profile. Since we are interested in large-scale structures, it is very unlikely to avoid the effect of the galactic mask in the analysis of the peaks. In this section, we consider a real space approach, analysing 2-dimensional patches around the peaks in a pixel-based formalism. This allows

one to take into account the mask in a simple way, as compared with the Fourier analysis provided by the multipolar profiles.

As in the previous sections, the patches around the peaks are parametrized by the polar coordinates (θ, ϕ) with the peak located at the centre of the system of reference. If the peak is described by its derivatives up to second order, the mean value of the field is given as Fourier expansion in terms of the multipolar profiles with $m = 0, 1, 2$ [31]:

$$\langle T(\theta, \phi) \rangle = \langle T_0(\theta) \rangle + \langle T_1(\theta) \rangle e^{i\phi} + \langle T_1^*(\theta) \rangle e^{-i\phi} + \langle T_2(\theta) \rangle e^{i2\phi} + \langle T_2^*(\theta) \rangle e^{-i2\phi} \quad (5.1)$$

On the other hand, the covariance of the temperature around the peak can be decomposed in terms of the intrinsic covariance of the field, and the covariance due to the effect of the peak selection [31]:

$$C(\theta, \phi, \theta', \phi') = C_{\text{intr.}}(\theta, \phi, \theta', \phi') + C_0^{\text{peak}}(\theta, \theta') + 2C_1^{\text{peak}}(\theta, \theta') \cos(\phi - \phi') + 2C_2^{\text{peak}}(\theta, \theta') \cos[2(\phi - \phi')], \quad (5.2)$$

where $C_{\text{intr.}}$ is the standard correlation function between the points (θ, ϕ) and (θ', ϕ') of the temperature field, which does not consider the contribution of the peak, and C_m^{peak} for $m = 0, 1, 2$ (defined in eq. (3.6)) represents the contribution to the covariance due to the fact that we are conditioning to the values of the derivatives at the location of the peak.

The data used to study the peaks directly in the real space are the Planck SEVEM and SMICA temperature maps, masked with their confidence masks [33]. The analysis of the 2-dimensional patches is based on the HEALPix pixelization scheme [40] of the regions around the peaks. For the largest peaks labelled by 1-4, the CMB data is filtered with a Gaussian of FWHM 2° in harmonic space and mapped at the resolution corresponding to $N_{\text{side}} = 32$. On the other hand, the Cold Spot (peak 5) is analysed at $N_{\text{side}} = 64$ with a FWHM of 1° . The masks for the two resolutions are calculated by smoothing the full resolution mask with the corresponding Gaussian, and masking pixels below a given threshold (in our case, 0.9). The resulting patches consist in disc-shape regions centred at the peaks with maximum radii of 60° for the largest peaks, and 30° for the Cold Spot, which leads to a total number of pixels ~ 3000 for each of the peaks. The gnomonic-projected CMB data at the peaks locations are represented in figure 8. Finally, the covariance and the theoretical profiles are calculated by using eqs. (3.6) and (3.2), where, as in the case of the multipolar profiles, the window function b_ℓ is given by the map resolution considered and the pixel window function.

The patches obtained from the data are compared with the theoretical models of the peaks obtained after conditioning to the values of the derivatives at the centre. The goodness of fit is evaluated by using a χ^2 test as a function of the maximum value of the radius considered in the analysis. No significant deviations from the theoretical models are found in the data for any of the peaks, a result which is consistent with the analysis of the multipolar profiles in Section 3. Finally, in order to check the consistency between the real space and multipolar profile methodologies, the analysis of patches is repeated with the full-sky Commander map, finding that both analysis are compatible with the standard model.

6 Conclusions

In this work, we have studied the most prominent large-scale peaks in the CMB temperature in terms of the multipolar profiles for different values of m . Since the peaks are characterized by their derivatives up to second order at the centre, we pay special attention to the monopolar and quadrupolar profiles, which have expectation values different from zero in this

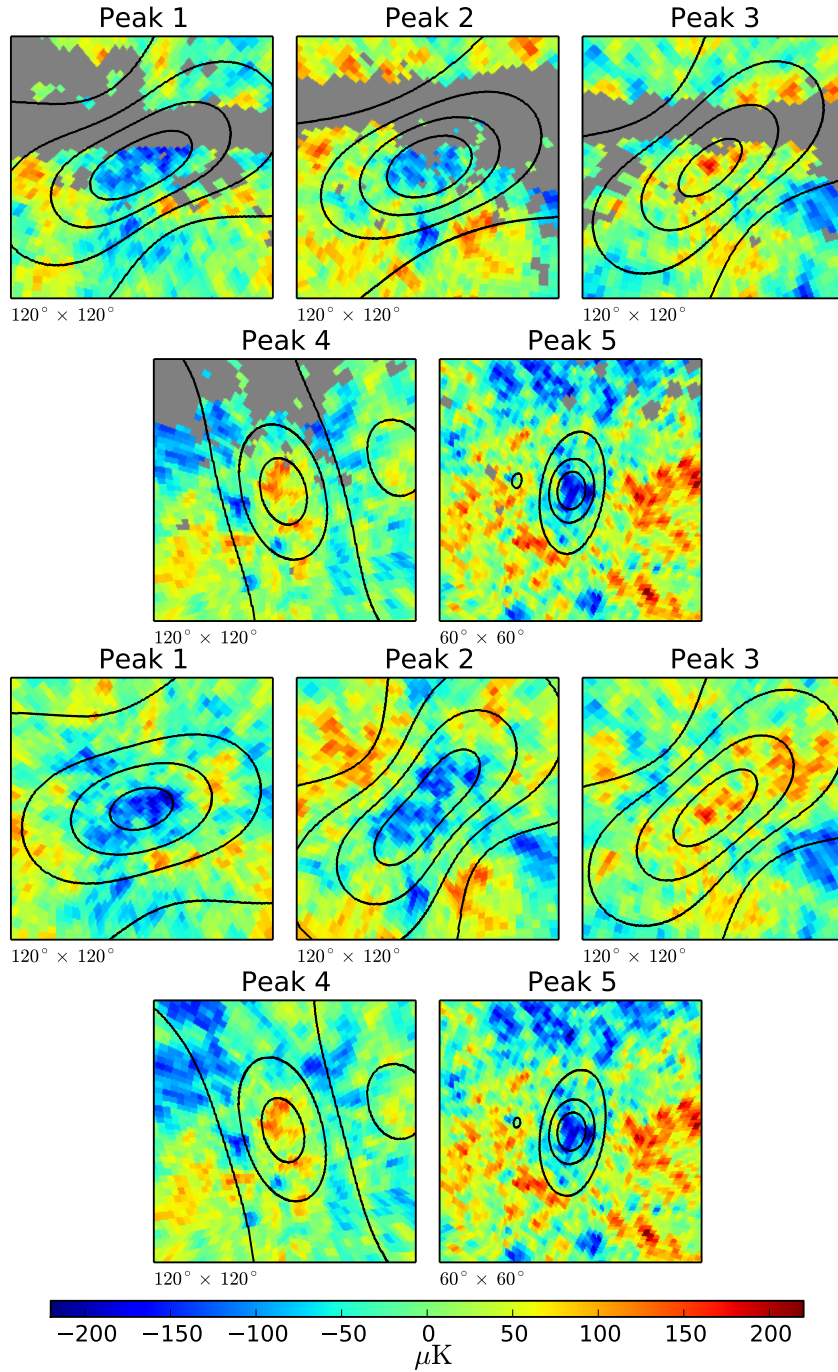


Figure 8. Temperature patches of the Planck SEVEM (first and second rows) and Commander (third and fourth rows) maps around the peaks considered in the 2-dimensional analysis, where, in the case of SEVEM, the missing pixels due to the galactic mask are represented in gray. The contours depicts the theoretical mean temperature field obtained by conditioning the values of the derivatives at the centre of the peak.

situation. Once the theoretical mean profiles and covariances are calculated by conditioning

the derivatives to the observed values, a χ^2 test is performed for each peak and value of m . The analysis suggests that the theoretical monopolar and quadrupolar profiles derived from the standard model present a good agreement with the profiles obtained from the data. Moreover, a broader analysis of the multipolar profiles concludes that there is no significant deviations in the profiles with m up to 10. These results implies that there is no anomalies in the shape of the peaks considered, at least once the values of the derivatives are conditioned.

The Cold Spot anomaly previously described in [24] is considered as a deviation in the Laplacian of the temperature field at the smoothing scale $R = 5^\circ$. The analysis performed by conditioning both the peak height ν and the curvature κ does not indicate any anomaly in the Cold Spot monopolar profile, but, on the other hand, if only the value of ν is fixed, the profile exhibits a 4.7σ deviation up to a radius $\theta = 10^\circ$. This result shows that the Cold Spot anomaly is mainly caused by the extremely large value of κ at the centre, while the field around it seems to be compatible with the Gaussian correlations in the standard model. Moreover, it is observed that the hot ring in the Cold Spot around 15° is caused by a combination of the large value of κ with a comparatively small peak amplitude ν .

The study of the multipolar profiles is completed by analysing their phases, which take into account the orientation of the different multipolar shapes around the peaks. In general, even in the case of a statistically isotropic field, the phase of the multipolar profiles are correlated for different values of theta. For this reason, in the paper, it is introduced an estimator which associates a phase-independent profile $\hat{T}_m(\theta)$ to each multipolar profile $T_m(\theta)$, given a fiducial model for its covariance. This allows to define a Rayleigh random walk in terms of the phases of the profiles, which moves as the value of θ increases. Statistical deviations from the standard model are characterized by the total length travelled by the random walk at a given time. If the distance covered by the random walk associated to a given multipolar profile is too large (too small), it means that the corresponding multipolar profile of the peak has a correlation (anti-correlation) for different values of θ which is greater than the one expected in the standard model, and therefore the peak presents an alignment for that value of m not compatible with an isotropic field. Some alignments are observed in few multipolar profiles of some of the large-scale peaks considered. In particular, the Cold Spot presents an alignment of the $m = 5$ profiles which is maximum at the hot ring position (15°).

Finally, the peaks are directly analysed in the real space by considering 2-dimensional patches around them. This methodology allows to take into account a galactic mask, which cannot be done in the multipolar profile expansion due to the spurious signal introduced in that case. As in the profile analysis, the peak field is compared with the theoretical expectation when the derivatives of the peak are conditioned. In particular, the direction of the elongation of each peak is fixed according to the observed eccentricity tensor. In this case, the results are compatible with the ones obtained in the multipolar profile analysis, concluding that the effect of the mask does not change the main conclusions already found with the multipolar profiles of the large-scale peaks.

A Binning of the theoretical profiles

In order to compare with the data, the theoretical profiles have to be binned in intervals of θ . Since these profiles are expressed in terms of the associated Legendre functions, this operation

can be done by calculating the following indefinite integrals:

$$I_\ell^m = \int \bar{P}_\ell^m(x) dx = \sqrt{\frac{2\ell+1}{4\pi}} \sqrt{\frac{(\ell-m)!}{(\ell+m)!}} \int P_\ell^m(x) dx, \quad (\text{A.1})$$

where the normalised associated Legendre functions \bar{P}_ℓ^m are introduced in order to prevent from large numbers in the calculations. On the one hand, the integrals for $m = 0, 2$ are calculated from the Legendre polynomials [35]:

$$I_\ell^0(x) = \frac{1}{\sqrt{(2\ell+1)(2\ell+3)}} \bar{P}_{\ell+1}(x) - \frac{1}{\sqrt{(2\ell+1)(2\ell-1)}} \bar{P}_{\ell-1}(x), \quad (\text{A.2a})$$

$$I_\ell^2(x) = \frac{1}{\sqrt{(\ell+2)(\ell+1)\ell(\ell-1)}} \left[-2I_\ell^0(x) + (\ell+3)x\bar{P}_\ell(x) - (\ell+1)\sqrt{\frac{2\ell+1}{2\ell+3}}\bar{P}_{\ell+1}(x) \right]. \quad (\text{A.2b})$$

On the other hand, in the case of $m = 1$, the integral can be determined recursively following the expressions in [35]:

$$I_\ell^1(x) = \frac{\ell-2}{\ell+1} \sqrt{\frac{(2\ell+1)\ell(\ell-2)}{(2\ell-3)(\ell+1)(\ell-1)}} I_{\ell-2}^1(x) + \frac{1}{\ell+1} \sqrt{\frac{(2\ell+1)(2\ell-1)}{(\ell+1)(\ell-1)}} (1-x^2) \bar{P}_{\ell-1}^1(x), \quad (\text{A.3})$$

where the initial conditions are given by

$$I_1^1(x) = -\frac{1}{4} \sqrt{\frac{3}{2\pi}} \left[x\sqrt{1-x^2} + \arcsin x \right], \quad (\text{A.4a})$$

$$I_2^1(x) = \frac{2}{3} \sqrt{1-x^2} \bar{P}_2^2(x). \quad (\text{A.4b})$$

Finally, the averaged value of the associated Legendre function P_ℓ^m in the interval $[\theta_1, \theta_2]$ is expressed as

$$\frac{1}{\cos \theta_2 - \cos \theta_1} \int_{\cos \theta_1}^{\cos \theta_2} dx P_\ell^m(x) = \sqrt{\frac{4\pi}{2\ell+1}} \sqrt{\frac{(\ell+m)!}{(\ell-m)!}} \frac{I_\ell^m(\cos \theta_2) - I_\ell^m(\cos \theta_1)}{\cos \theta_2 - \cos \theta_1}. \quad (\text{A.5})$$

Alternatively, these integrals can be evaluated using numerical quadrature methods, but the recursive expressions above are faster and more accurate.

Acknowledgments

Partial financial support from the Spanish Ministerio de Economía y Competitividad Projects AYA2012-39475-C02-01 and Consolider-Ingenio 2010 CSD2010-00064 is acknowledged.

References

- [1] Planck Collaboration, P. A. R. Ade, N. Aghanim, M. Arnaud, M. Ashdown, J. Aumont, C. Baccigalupi, A. J. Banday, R. B. Barreiro, J. G. Bartlett, and et al., *Planck 2015 results. XIII. Cosmological parameters*, A&A **594** (Sept., 2016) A13, [[arXiv:1502.01589](https://arxiv.org/abs/1502.01589)].

- [2] D. N. Spergel, L. Verde, H. V. Peiris, E. Komatsu, M. R. Nolta, C. L. Bennett, M. Halpern, G. Hinshaw, N. Jarosik, A. Kogut, M. Limon, S. S. Meyer, L. Page, G. S. Tucker, J. L. Weiland, E. Wollack, and E. L. Wright, *First-Year Wilkinson Microwave Anisotropy Probe (WMAP) Observations: Determination of Cosmological Parameters*, ApJS **148** (Sept., 2003) 175–194, [[astro-ph/0302209](#)].
- [3] Planck Collaboration, P. A. R. Ade, N. Aghanim, Y. Akrami, P. K. Aluri, M. Arnaud, M. Ashdown, J. Aumont, C. Baccigalupi, A. J. Banday, and et al., *Planck 2015 results. XVI. Isotropy and statistics of the CMB*, A&A **594** (Aug., 2016) A16, [[arXiv:1506.07135](#)].
- [4] C. L. Bennett, M. Halpern, G. Hinshaw, N. Jarosik, A. Kogut, M. Limon, S. S. Meyer, L. Page, D. N. Spergel, G. S. Tucker, E. Wollack, E. L. Wright, C. Barnes, M. R. Greason, R. S. Hill, E. Komatsu, M. R. Nolta, N. Odegard, H. V. Peiris, L. Verde, and J. L. Weiland, *First-Year Wilkinson Microwave Anisotropy Probe (WMAP) Observations: Preliminary Maps and Basic Results*, ApJS **148** (Sept., 2003) 1–27, [[astro-ph/0302207](#)].
- [5] C. J. Copi, D. Huterer, D. J. Schwarz, and G. D. Starkman, *Lack of large-angle TT correlations persists in WMAP and Planck*, MNRAS **451** (Aug., 2015) 2978–2985, [[arXiv:1310.3831](#)].
- [6] C. Monteserín, R. B. Barreiro, P. Vielva, E. Martínez-González, M. P. Hobson, and A. N. Lasenby, *A low cosmic microwave background variance in the Wilkinson Microwave Anisotropy Probe data*, MNRAS **387** (June, 2008) 209–219, [[arXiv:0706.4289](#)].
- [7] M. Cruz, P. Vielva, E. Martínez-González, and R. B. Barreiro, *Anomalous variance in the WMAP data and Galactic foreground residuals*, MNRAS **412** (Apr., 2011) 2383–2390, [[arXiv:1005.1264](#)].
- [8] C. R. Contaldi, M. Peloso, L. Kofman, and A. Linde, *Suppressing the lower multipoles in the CMB anisotropies*, J. Cosmology Astropart. Phys. **7** (July, 2003) 002, [[astro-ph/0303636](#)].
- [9] C. Destri, H. J. de Vega, and N. G. Sanchez, *Preinflationary and inflationary fast-roll eras and their signatures in the low CMB multipoles*, Phys. Rev. D **81** (Mar., 2010) 063520, [[arXiv:0912.2994](#)].
- [10] C. J. Copi, D. Huterer, D. J. Schwarz, and G. D. Starkman, *Large-scale alignments from WMAP and Planck*, MNRAS **449** (June, 2015) 3458–3470, [[arXiv:1311.4562](#)].
- [11] Planck Collaboration, P. A. R. Ade, N. Aghanim, C. Armitage-Caplan, M. Arnaud, M. Ashdown, F. Atrio-Barandela, J. Aumont, C. Baccigalupi, A. J. Banday, and et al., *Planck 2013 results. XXIII. Isotropy and statistics of the CMB*, A&A **571** (Nov., 2014) A23, [[arXiv:1303.5083](#)].
- [12] H. K. Eriksen, F. K. Hansen, A. J. Banday, K. M. Górski, and P. B. Lilje, *Asymmetries in the Cosmic Microwave Background Anisotropy Field*, ApJ **605** (Apr., 2004) 14–20, [[astro-ph/0307507](#)].
- [13] F. K. Hansen, A. J. Banday, K. M. Górski, H. K. Eriksen, and P. B. Lilje, *Power Asymmetry in Cosmic Microwave Background Fluctuations from Full Sky to Sub-Degree Scales: Is the Universe Isotropic?*, ApJ **704** (Oct., 2009) 1448–1458, [[arXiv:0812.3795](#)].
- [14] C. Gordon, *Broken Isotropy from a Linear Modulation of the Primordial Perturbations*, ApJ **656** (Feb., 2007) 636–640, [[astro-ph/0607423](#)].
- [15] J. Hoftuft, H. K. Eriksen, A. J. Banday, K. M. Górski, F. K. Hansen, and P. B. Lilje, *Increasing Evidence for Hemispherical Power Asymmetry in the Five-Year WMAP Data*, ApJ **699** (July, 2009) 985–989, [[arXiv:0903.1229](#)].
- [16] K. Land and J. Magueijo, *Is the Universe odd?*, Phys. Rev. D **72** (Nov., 2005) 101302, [[astro-ph/0507289](#)].
- [17] J. Kim and P. Naselsky, *Anomalous parity asymmetry of WMAP 7-year power spectrum data*

- at low multipoles: *Is it cosmological or systematics?*, Phys. Rev. D **82** (Sept., 2010) 063002, [[arXiv:1002.0148](#)].
- [18] A. Gruppuso, F. Finelli, P. Natoli, F. Paci, P. Cabella, A. de Rosa, and N. Mandolesi, *New constraints on parity symmetry from a re-analysis of the WMAP-7 low-resolution power spectra*, MNRAS **411** (Mar., 2011) 1445–1452, [[arXiv:1006.1979](#)].
- [19] P. Naselsky, W. Zhao, J. Kim, and S. Chen, *Is the Cosmic Microwave Background Asymmetry due to the Kinematic Dipole?*, ApJ **749** (Apr., 2012) 31.
- [20] W. Zhao, *Directional dependence of CMB parity asymmetry*, Phys. Rev. D **89** (Jan., 2014) 023010, [[arXiv:1306.0955](#)].
- [21] J. Kim and P. Naselsky, *Lack of Angular Correlation and Odd-parity Preference in Cosmic Microwave Background Data*, ApJ **739** (Oct., 2011) 79, [[arXiv:1011.0377](#)].
- [22] C. J. Copi, D. Huterer, D. J. Schwarz, and G. D. Starkman, *On the large-angle anomalies of the microwave sky*, MNRAS **367** (Mar., 2006) 79–102, [[astro-ph/0508047](#)].
- [23] P. Vielva, E. Martínez-González, R. B. Barreiro, J. L. Sanz, and L. Cayón, *Detection of Non-Gaussianity in the Wilkinson Microwave Anisotropy Probe First-Year Data Using Spherical Wavelets*, ApJ **609** (July, 2004) 22–34, [[astro-ph/0310273](#)].
- [24] M. Cruz, E. Martínez-González, P. Vielva, and L. Cayón, *Detection of a non-Gaussian spot in WMAP*, MNRAS **356** (Jan., 2005) 29–40, [[astro-ph/0405341](#)].
- [25] C. L. Bennett, R. S. Hill, G. Hinshaw, D. Larson, K. M. Smith, J. Dunkley, B. Gold, M. Halpern, N. Jarosik, A. Kogut, E. Komatsu, M. Limon, S. S. Meyer, M. R. Nolta, N. Odegard, L. Page, D. N. Spergel, G. S. Tucker, J. L. Weiland, E. Wollack, and E. L. Wright, *Seven-year Wilkinson Microwave Anisotropy Probe (WMAP) Observations: Are There Cosmic Microwave Background Anomalies?*, ApJS **192** (Feb., 2011) 17, [[arXiv:1001.4758](#)].
- [26] A. Marcos-Caballero et al., *Multiscale analysis of the CMB temperature derivatives*, .
- [27] J. M. Bardeen, J. R. Bond, N. Kaiser, and A. S. Szalay, *The statistics of peaks of Gaussian random fields*, ApJ **304** (May, 1986) 15–61.
- [28] J. R. Bond and G. Efstathiou, *The statistics of cosmic background radiation fluctuations*, MNRAS **226** (June, 1987) 655–687.
- [29] R. B. Barreiro, J. L. Sanz, E. Martínez-González, L. Cayón, and J. Silk, *Peaks in the Cosmic Microwave Background: Flat versus Open Models*, ApJ **478** (Mar., 1997) 1–6, [[astro-ph/9612114](#)].
- [30] E. Komatsu, K. M. Smith, J. Dunkley, C. L. Bennett, B. Gold, G. Hinshaw, N. Jarosik, D. Larson, M. R. Nolta, L. Page, D. N. Spergel, M. Halpern, R. S. Hill, A. Kogut, M. Limon, S. S. Meyer, N. Odegard, G. S. Tucker, J. L. Weiland, E. Wollack, and E. L. Wright, *Seven-year Wilkinson Microwave Anisotropy Probe (WMAP) Observations: Cosmological Interpretation*, ApJS **192** (Feb., 2011) 18, [[arXiv:1001.4538](#)].
- [31] A. Marcos-Caballero, R. Fernández-Cobos, E. Martínez-González, and P. Vielva, *The shape of CMB temperature and polarization peaks on the sphere*, J. Cosmology Astropart. Phys. **4** (Apr., 2016) 058, [[arXiv:1512.07412](#)].
- [32] E. Martínez-González, J. E. Gallegos, F. Argüeso, L. Cayón, and J. L. Sanz, *The performance of spherical wavelets to detect non-Gaussianity in the cosmic microwave background sky*, MNRAS **336** (Oct., 2002) 22–32, [[astro-ph/0111284](#)].
- [33] Planck Collaboration, R. Adam, P. A. R. Ade, N. Aghanim, M. Arnaud, M. Ashdown, J. Aumont, C. Baccigalupi, A. J. Banday, R. B. Barreiro, and et al., *Planck 2015 results. IX. Diffuse component separation: CMB maps*, A&A **594** (Aug., 2016) A9, [[arXiv:1502.05956](#)].

- [34] M. Cruz, M. Tucci, E. Martínez-González, and P. Vielva, *The non-Gaussian cold spot in WilkinsonMicrowaveAnisotropyProbe: significance, morphology and foreground contribution*, MNRAS **369** (June, 2006) 57–67, [[astro-ph/0601427](#)].
- [35] A. R. DiDonato, *Recurrence relations for the indefinite integrals of the associated legendre functions*, *Mathematics of Computation* **38** (1982), no. 158 547–551.
- [36] A. Kovács, I. Szapudi, and Z. Frei, *Phase statistics of the WMAP 7 year data*, *Astronomische Nachrichten* **334** (Nov., 2013) 1020, [[arXiv:1308.0837](#)].
- [37] A. Stannard and P. Coles, *Random-walk statistics and the spherical harmonic representation of cosmic microwave background maps*, MNRAS **364** (Dec., 2005) 929–933, [[astro-ph/0410633](#)].
- [38] J. R. Gott, W. N. Colley, C.-G. Park, C. Park, and C. Mugnolo, *Genus topology of the cosmic microwave background from the WMAP 3-year data*, MNRAS **377** (June, 2007) 1668–1678, [[astro-ph/0610764](#)].
- [39] K. Mardia and P. Jupp, *Directional Statistics*. Wiley Series in Probability and Statistics. Wiley, 2009.
- [40] K. M. Górski, E. Hivon, A. J. Banday, B. D. Wandelt, F. K. Hansen, M. Reinecke, and M. Bartelmann, *HEALPix: A Framework for High-Resolution Discretization and Fast Analysis of Data Distributed on the Sphere*, ApJ **622** (Apr., 2005) 759–771, [[astro-ph/0409513](#)].